CO_2 SELECTIVE CERAMIC MEMBRANE FOR WATER-GAS SHIFT REACTION WITH CONCOMITANT RECOVERY OF CO_2

Annual Report for the Period September 1, 2000 to August 31, 2001

Paul K. T. Liu
Project Director

MEDIA AND PROCESS TECHNOLOGY, INC.

September 30, 2001

PREPARED FOR THE UNITED STATES
DEPARTMENT OF ENERGY
Under Cooperative Agreement
No. DE-FC26-00NT40922

Technical Summary

During Year I this project has been focused on the two topic areas below:

(i) understanding comprehensively the CO_2 affinity vs temperature, reversibility of CO_2 affinity, and the role of water in order to select an optimum hydrotalcite composition for membrane preparation, and

(ii) developing a membrane synthesis protocol for depositing the hydrotalcite material into a commercially available ceramic membrane from us.

This annual report documents the progress we have made in these areas.

Bulk hydrotalcite materials were successfully prepared. The Al/(Al + Mg) ratio is within the range reported in the literature. Further their XRD and TGA patterns are consistent with the characteristics of hydrotalcite materials reported in the literature. This preparation method has been incorporated into the protocol for membrane synthesis.

Our study using TG/MS concludes that the CO_2 affinity of the hydrotalcite material is reversible at ~200ºC and in the presence of water. Surface study via FTIR, DRIFTS and TGA/MS have been used to quantitatively characterize the thermal behavior of the hydrotalcite material. Based upon these characterization results, a thermal evolution pattern accounting for the loss of interlayer water, hydroxyl group, and CO_2 is proposed for the hydrotalcite we studied. A small amount of CO_2 release (~2wt%) was observed at ~220ºC, while the remaining releases at ~450ºC. Both regions are possible candidates for transport of CO_2 in a membrane configuration. Presently, we are conducting high-pressure adsorption/desorption study to verify the reversibility of the CO_2 released from these two regions at the proposed operating condition.

A multi-faucet approach has been taken to develop the membrane synthesis technique we proposed. An in-situ crystallization technique has been developed, which can deposit hydrotalcite (in the range of 0. 1 μm) into the inner surface of the ceramic tube as substrate. Permeance and pore size distribution analysis indicate that about 50-60 % of the original pore volume of the substrate was deposited with the single crystal of hydrotalcite. SEM and EDX analysis exhibit the presence of a hydrotalcite thin layer within the top surface of the substrate. In year II we will conduct a thorough analysis to determine the depth of the hydrotalcite crystallization penetration for future optimization study.

In addition a post treatment technique via chemical vapor deposition/infiltration (CVI) has been developed. This technique can back patch the pore opening remained from the deposition. About 75% residual pore volume was plugged with this CVI technique in a preliminary study. SEM/EDX analysis shows that no additional layer thickness resulted from the CVI back patching, indicating that the pore plugging take place within the porous structure of the substrate. Thus, it is believed that the CVI technique developed satisfies our performance requirement, specifically, penetration and plugging of the pore openings without indiscriminate deposition of an over layer on the top of the existing substrate. An optimization study will be focused in Year II to complete the pore plugging. The performance of the hydrotalcite membrane thus prepared was characterized in terms of its CO_2 permeance enhancement. At 300 C, the CO_2 permeance doubled as a result of the enhancement of the hydrotalcite embedded in the pores. Active transport of CO_2 via the hydrotalcite membrane is clearly demonstrated in the membrane we prepared.

In summary, the Year I study has demonstrated the technical feasibility of preparing a hydrotalcite. The proposed membrane synthesis protocol will be refined and optimized in Year II. In addition, surface analysis techniques employing FTIR and DRIFTS have been developed. These techniques have been applied to a hydrotalcite model compound to demonstrate our ability to screen hydrotalcite materials in terms of its composition and % of cation substitution. These techniques will be utilized in Year II to formulate an optimized hydrotalcite candidate for preparing a membrane with maximized CO_2 transport at the proposed process condition.

TABLE OF CONTENTS

1. Hydrotalcite (Bulk Material) Synthesis and Characterization

The first step of this project was to identify the conditions for the formation of hydrotalcite material. A commonly discussed Al/Mg hydrotalcite was chosen for this study. In addition, the crystal growth kinetics, such as size and rate vs time, are essential background information for us to develop a hydrotalcite membrane synthesis technique. The conditions we chose for the formation of hydrotalcite were well documented in the literature [2]. However, no literature data known to us deals with the crystal size and growth rate. Our objective here is to establish the crystal growth kinetics from a simple empirical study, while leaving the comprehensive study in the future. Crystal formation and its characterization are presented in this section. The crystal growth rate and size are discussed in the next section.

Experimental

1. Hydrotalcite crystals were formed by adding the equal volumes of $AlCl_3$ (0.073 mole/l) and $MgCl_2$ (0.28 mole/l) to a Na_2CO_3 solution (0.25 mole/l) at room temperature and a pH of ca. 11.5 under a well mixed condition. To increase the crystal size, we also allowed the mixture to age under a well-mixed condition for up to 72 hours. The crystals thus formed were isolated via filtration and then rinsed thoroughly with water to remove residual sodium, carbonate, and chloride.

2. The composition of the precipitate was analyzed by Direct Current Plasma (DCP) spectrophotometer to determine the relative ratio of Mg to Al. In addition, the precipitate after drying was characterized by XRD and TGA/DTG for comparison with the literature.

Results

1. Al and Mg contents of the precipitates are summarized in Table 1.1. The Al/(Al + Mg) ratio reported here is within the range reported in the literature of up to 0.45 [4]. The difference between the two samples is most likely attributed to the completeness of the crystal formation as a function of the aging time.

2. The XRD of a representative precipitate is shown in Figure 1.1. Characteristic peaks of hydrotalcite obtained in the literature [1] is inserted in this figure for comparison. These peaks are all present in our precipitate.

3. The weight loss vs temperature of the precipitate is obtained from a TGA/DTG study as shown in Figure 1.2. According to the literature, three major weight loss peaks are observed represented by (i) inter layer water loss, (ii) intracrystal water loss, and/or (iii) carbonate ion loss. The weight loss of our material shown in Figure 2 is consistent with the literature data [1,3,4]. Surface characterization of this material is presented in Sec. 8.

Conclusions/Implications

1. Based upon the composition analysis, XRD pattern, and TGA/DTG curve, it is believed that the protocol we adopted here produces typical hydrotalcite crystals. This protocol can be incorporated into the hydrotalcite membrane synthesis (see Sec. 3 & 4).

Table 1.1 Summary of the aluminum and magnesium contents of the precipitate after ten minutes and six hours of mixing.

Sample ID	#1	#2
Comments [-]	Sample collected after 10 minutes of mixing.	Sample collected after 6 hours of mixing.
Al [ppm]	1.82	1.03
Mg [ppm]	3.07	2.28
Al/(Al + Mg)[mole fraction, experimental]	0.40	0.29
Al/(Al + Mg) [stochiometric]	0.21	0.21

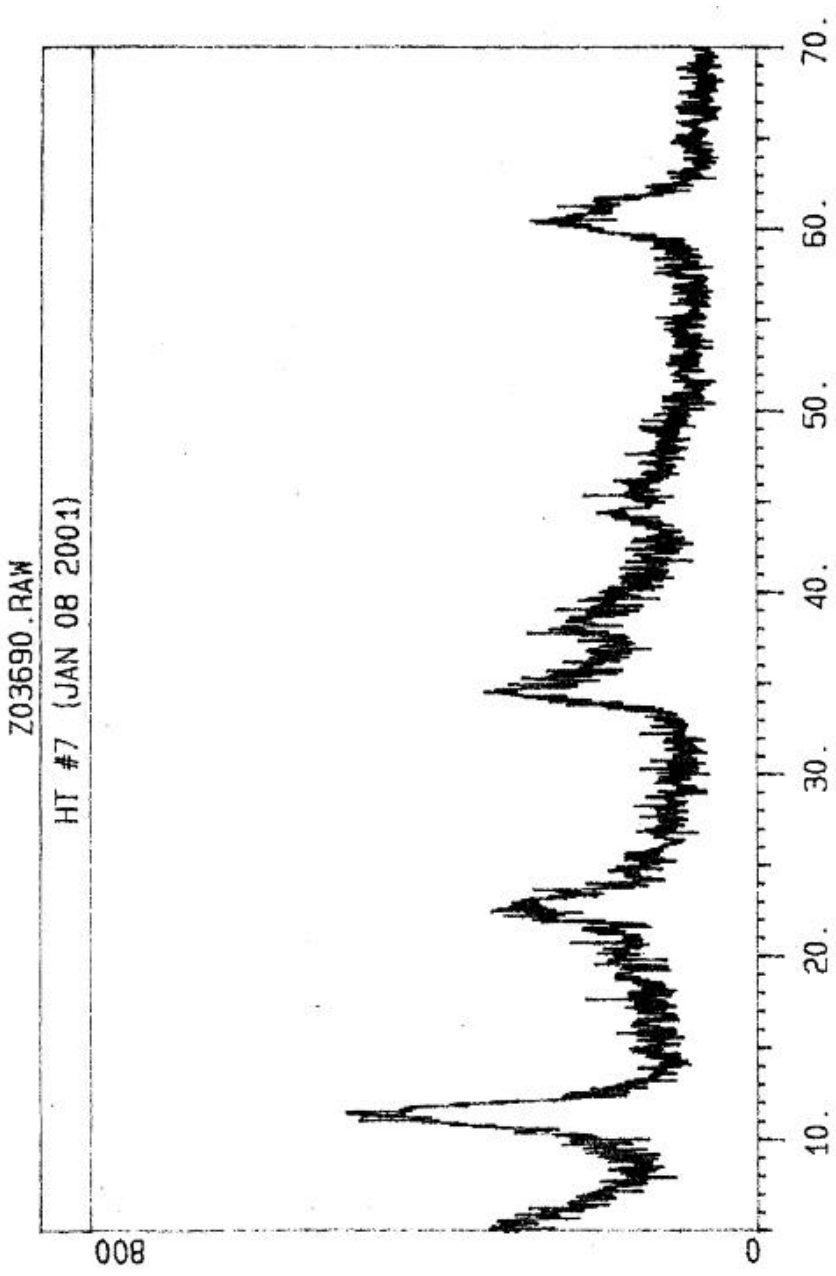

Figure 1. XRD pattern for hydrotalcite prepared under this project. Inset shows the XRD pattern for a hydrotalcite sample from the literature for comparison.

Figure 1.1 XRD pattern for hydrotalcite prepared under this project. Inset shows the XRD tern for a hydrotalcite sample from the literature for comparison.

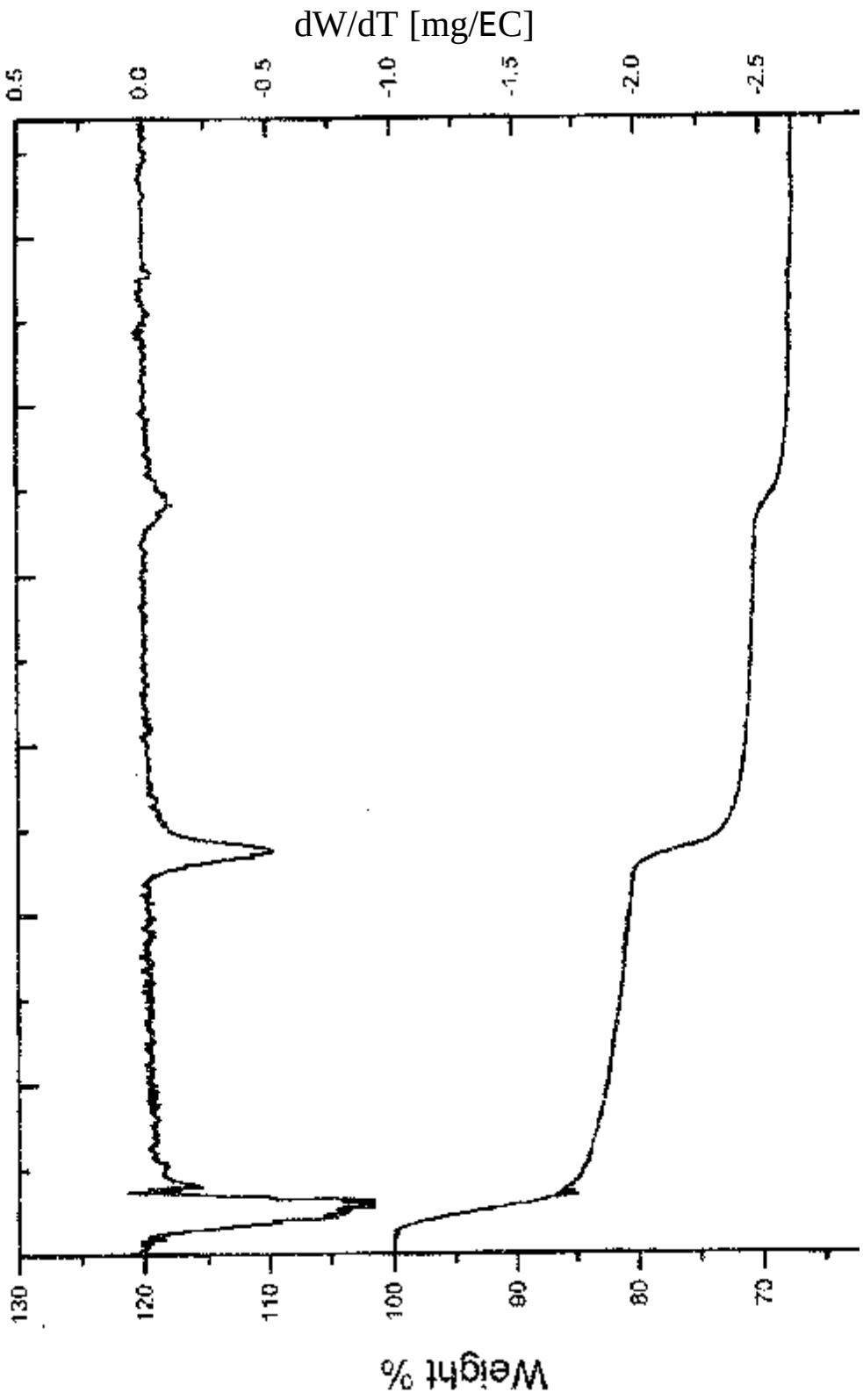

Figure 1..2. TGA/DTG thermogram hydrotalcite prepared under this project.

2. Hydrotalcite Crystal Size and Growth Rate

As stated in the preceding section, information on the crystal growth rate and size are essential for us to develop a hydrotalcite membrane. Once this is accomplished, an appropriate substrate pore size and crystal growth time and conditions for membrane synthesis can be selected. Since no literature data is available in this specific topic, we have taken an empirical approach to generate the required information, which is discussed below.

Two literature reports indicate that aging is required in order to increase the crystal size [3, 5]. We will confirm this crystal growth condition and its size with bulk material first. Then, the growth condition and technique will be adapted as a 2^{nd} step of our membrane synthesis technique.

Experimental

1. An empirical approach has been designed by us, specifically, to characterize the crystal size formation vs time during the hydrotalcite crystal growth. Our commercial ceramic membranes with well defined pore sizes were used as filters to gauge the crystal size while the crystal population density was determined by turbidity and Al and Mg concentration measurements. Both 0.2μm and 500D pore size membranes were selected as first candidates for this study.

2. In a separate study, crystal growth, not formation, is focused. The hydrotalcite solution after adding together the major components is aged at 75 C for up to 15 days to increase the crystal growth under this selected condition. The crystals after recovered are subject to XRD and TEM analyses. The sharpness of the XRD peak will offer an indication of the crystal size, while the TEM will offer a direct measurement of the crystal size.

Results

1. It was found that the hydrotalcite formed immediately following addition of the $AlCl_3/MgCl_2$ solution to the Na_2CO_3 solution. The turbidity of the solution increases almost instantaneously while very little turbidity is detected in the filtrate from the membrane (see Table 2.1 at time $198min). Furthermore, the magnesium concentration in the membrane filtrate is extremely low in comparison with the feed. This indicates that little Mg has permeated the membrane either as hydrotalcite crystals or as Mg ions. Hence, all of the magnesium is incorporated very rapidly into hydrotalcite crystal formation. The fact that the aluminum concentration in the permeate is relatively constant (but the permeate turbidity is low) indicates that not all of the aluminum ions have been incorporated in the hydrotalcite crystals. Finally, the hydrotalcite crystal size formed is likely /0.1Fm, since the crystals formed were nearly completely rejected by the 0.2Fm membrane. These results indicate that hydrotalcite crystal formation and growth is very rapid, occurring in the initial mixing (see Table 2.1) for the experimental conditions we selected.

2. The crystal growth experiment is underway. The initial result shows that the crystal formed initially after the solution is formed is likely very fine because its XRD peak is broader than those reported in the literature. We are currently preparing the sample aged for 15 days and waiting for the TEM analysis.

Implications/Conclusions

1. Our study suggests that the hydrotalcite crystals nucleate and grow very rapidly to a size /0.1Fm, if they can be forced to nucleate in the membrane pores, it is possible that single crystals can be embedded in each of the pores at the surface of the 0.2Fm membrane. The in-situ crystallization (ISC) technique discussed in the next section offers one method to achieve this goal. Single crystals embedded in the pores is the ideal morphology for the hydrotalcite membrane. This morphology would yield continuous CO_2 transport channels (within a single crystal) and deliver a high quality membrane capable of achieving very high CO_2 permselectivities.

Table 2.1: Permeation Rate and Feed and Permeate Characteristics of 0.2 μm Membrane Before and After Addition of the Al/Mg Stock Solution to Form Hydrotalcite. Feed Recirculation Rate is ca. 1 liter/min. Feed Volume is 500cc.

Time [min]	Permeation Rate [cc/min]	Feed Turbidity [NTU]	Permeate Turbidity [NTU]	Feed Aluminum [ppm]	Permeate Aluminum [ppm]	Feed Magnesium [ppm]	Permeate Magnesium [ppm]
0	19.67						
193	18.46						
198	Add 5 cc of stock Mg/Al solution						
200	15.16	9.8	0.05	26.2	4.74	5.20	0.4
211	15.33						
290	17.60	6.3	0.36	23.9	4.80		
399	15.60						
430	16.90			14.8	3.3	1.69	0

3. In-situ Crystallization for Hydrotalcite Membrane Synthesis

The result from Sec. 2 suggests the possibility that hydrotalcite crystals in the neighborhood of 0.1Fm or greater are immediately formed when the two solutions are combined together. The conventional approach (such as methods developed for the zeolitic membrane) involving the deposition of pre-formed crystals as seeds for crystal growth within the porous structure of the membrane becomes unnecessary. It is feasible to form a single crystal of hydrotalcite within the membrane porous structure if the two reactants (i.e., Na_2CO_3 and $AlCl_3/MgCl_2$) can be combined together within the porous structure. This rationale represents a major breakthrough, which can eliminate many tedious steps in the crystal formation as in the zeolitic membrane development. A two-phase contactor using the membrane as an interphase appears to be an ideal device for us to achieve immediate crystal formation within the porous structure of the membrane. To demonstrate feasibility, a batch type two phase contactor was used to simplify the equipment design, acquisition and set-up.

Experimental

1. As an initial attempt, we filled the tube side of a membrane plugged at one end with one of the reactants, $AlCl_3/MgCl_2$, thereby completely wetting the pores of the substrate with the reactant. Then, the tube was dipped into a batch of well-mixed Na_2CO_3 solution. This approach was anticipated to embed hydrotalcite crystals in the pores of the support near the outer tubular surface, because the two solutions in contact at the membrane surface are stagnant and hence do not intermix rapidly.

2. Two membranes with 500D and 0.2Fm pore sizes were selected as candidate substrates for this study. These "-Al_2O_3-based membranes are ideal for this application due to their chemical resistance to the high pH of the Na_2CO_3 solution (11 to 12). Each tubular membrane was 10" long, 5.5mm OD and 3.5mm ID with one end plugged with epoxy to hold the $AlCl_3/MgCl_2$ solution.

3. The tube was left in the batch solution for 0.5 to 1 hour to assure complete crystal formation. Then the tube was withdrawn and thoroughly rinsed with water and then dried. As part of the feasibility study, this crystal formation step was repeated up to 3 times to study the degree of crystal embedding/coverage. Thus 3 samples were generated for each membrane pore size.

Results

1. Evidently the hydrotalcite crystal was formed within the porous structure of the "-Al_2O_3 substrate based upon (i) the significant reduction in permeance of He and N_2 as shown in Table 3.1, (ii) the increase in the selectivity of He/N_2 (Table 3.1), and (iii) the reduction in the pore size and/or pore volume (Figure 3.1). As expected, the pore size reduction for the 0.2Fm membrane was substantial, specifically, from 0.2Fm to 0.15, 0.08, and 0.05Fm for the 1^{st}, 2^{nd}, and 3^{rd} deposition cycles, respectively. The increase in selectivity and reduction in the permeance are supportive of the pore size reduction by the in-situ formation of the hydrotalcite crystal.

2. SEM photomicrographs of the inner and outer tubular surface of the 0.2Fm membrane after in-situ crystal formation are presented in Figure 3.1. Clearly, no plugging of the inner surface of the membrane was observed. The pore plugging was clearly shown in the outer tubular surface under both low (Figure 3.2) and high magnification (Figure 3.3). EDX mapping shown in Figure 3.4 confirms the formation of the hydrotalcite crystals.

3. The penetration of the crystal is believed to be very limited, since the microporous structure of the cross section of the membrane did not exhibit any deposition even near the outer tubular surface (see Figure 3.3). On the other hand, crystal spill-over to the top of the outer tubular surface is believed to be minimal because the surface topography of the substrate is still visible as indicated by the absence of Mg in these areas (see Figure 3.4). Thus, the morphological evidence indicates that the proposed synthesis protocol delivers an ultrathin hydrotalcite patch within the pores very near the surface of the substrate with little or no excess crystal formation on the surface via the proposed synthesis protocol.

4. A similar result was obtained with the 500D substrate shown in Figure 3.5. The pore size reduction in this case was not as obvious as that for the 0.2Fm substrate; however, it is obvious that the pore volume is reduced

dramatically by the crystals because of the large reduction in gas permeability of the membrane shown in Table 3.1.

5. Repeated additional depositions of the hydrotalcite crystals further reduced the permeance and pore size. It is believed that the additional depositions resulted in further infiltration of the residual pore openings that remained due to incomplete or non-uniform coverage from previous depositions. However, the majority of the crystals were embedded in the substrate during the 1st deposition cycle based upon the dramatic permeance reduction after the first cycle. This phenomenon is obvious for the 0.2 μ membrane while no pore size distribution evidence is obtained to support this claim for 500Å membrane.

Conclusions/Implications

1. The crystals are clearly embedded within the openings of the porous structure of the substrate. The residual pore volume with pore sizes in the range of <20Å to ca. 500Å is small enough that it can be used as seed for crystal growth or directly back-patched using our CVI technique (see Sec. 5).

2. Optimization of the two phase contactor technique is highly recommended in the future, particularly modification of the technique developed here for deposition of the crystal in the inner tubular surface. Our 1st generation of the hydrosulfite membrane will be deposited in the inner tubular surface due to the convenience and the ease of technical development. Sec. 4 addresses this issue.

Table 3.1: Permeance and Selectivity of the 500Å and 0.2μm Pore Size Ceramic Substrates Following In-situ Deposition/Crystal Growth of Hydrotalcite within the Pores. Based Upon the SEM Analysis, Crystal Growth is Concentrated at the Surface of the Membrane.

Pore Size of Substrate [μm]	Times of Deposition [-]	Permeance [$m^3/m^2/hr/bar$] @ 25°C		Ideal Selectivity [-]	Remarks
		Helium	Nitrogen		
0.05	0	81.2	41.5	1.96	control
0.05	1	2.04	0.913	2.24	
0.05	2	-	-	-	
0.05	3	5.22	2.35	2.22	
02	0	113	66.3	1.70	control
0.2	1	18.8	11.2	1.68	
0.2	2	-	-	-	
0.2	3	15.0	6.52	2.30	

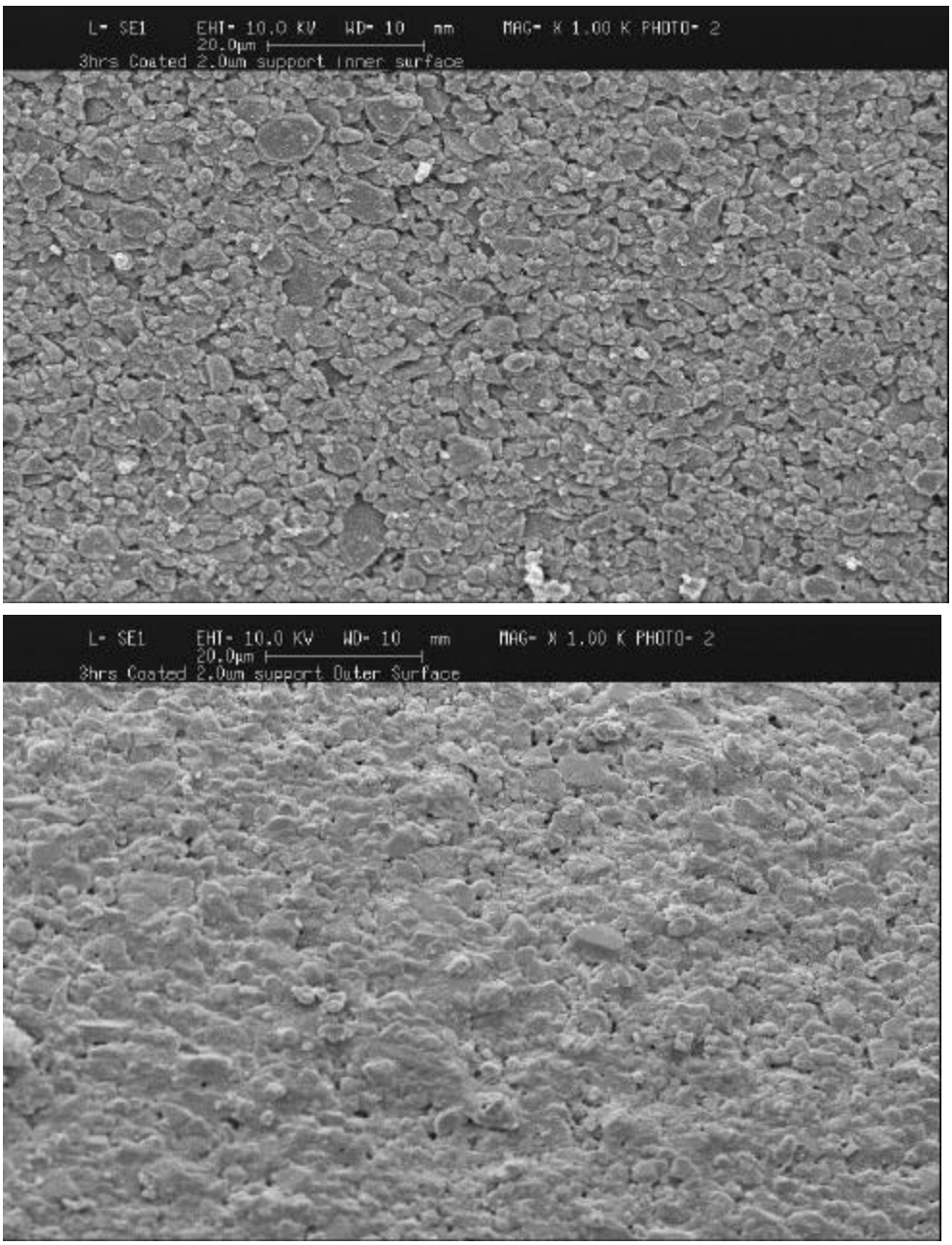

Figure 3.1 SEM Photomicrograph of 0.2µ substrate after in-situ crystallization of hydrotalcite: inner tubular surface (top), and outer tubular surface (bottom). Pore plugging by hydrotalcite on the outer tubular surface is evident.

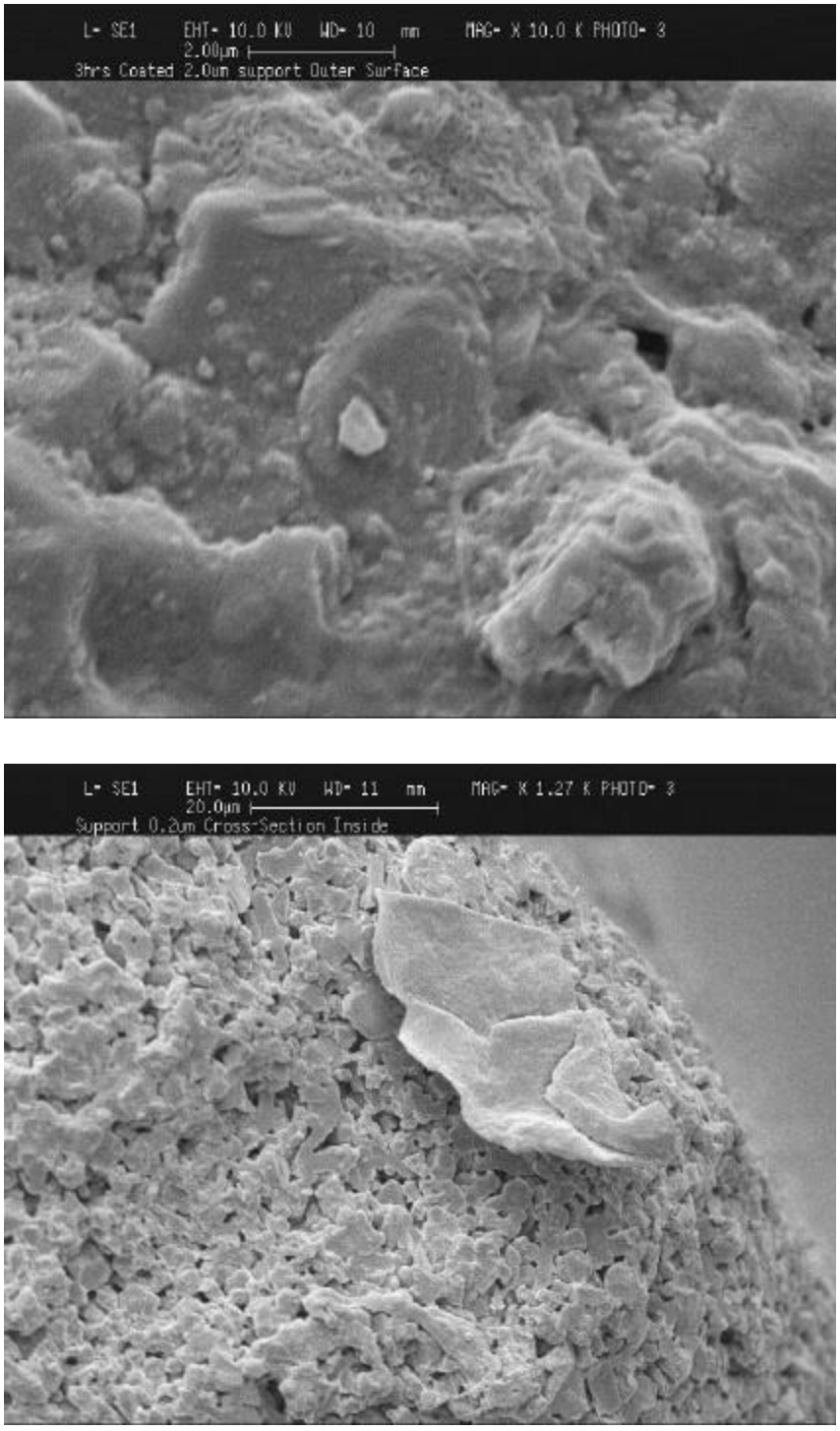

Figure 3.2: SEM Photomicrograph of the outer tubular surface (top) and cross section (bottom) of the 0.2µm substrate, (Figure 3.2 under a higher magnification). Pore plugging by the hydrotalcite is evident under this higher magnification on the outer surface but not in the cross section.

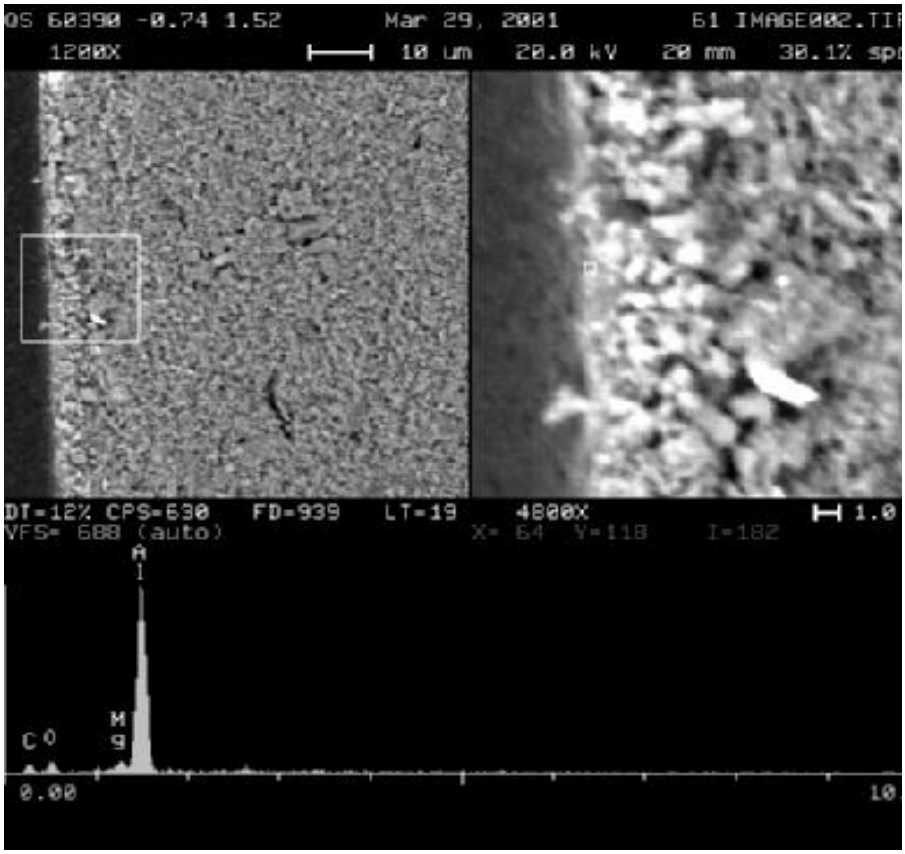

Figure 3.3 SEM Photomicrograph and EDX of the outer surface of the 500Å substrate after in-situ crystallization of hydrotalcite. The presence of Mg confirms the formation of hydrotalcite on the outer tubular surface.

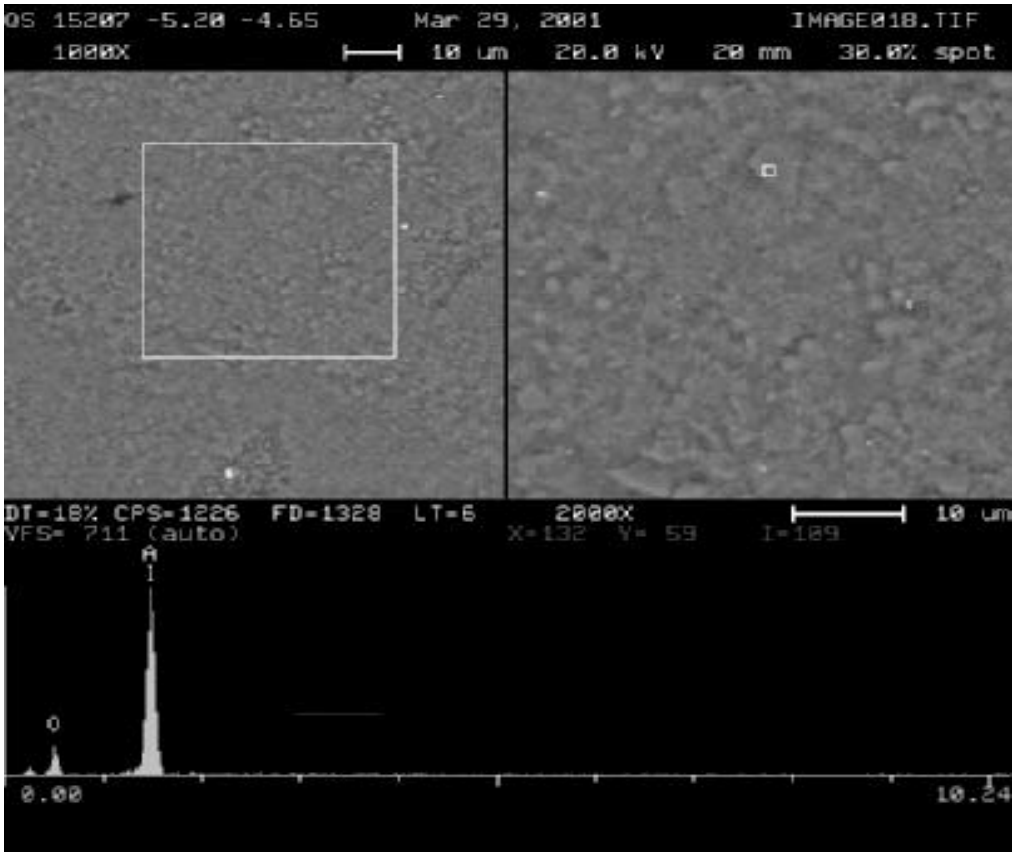

Figure 3.4	SEM Photomicrograph and EDX focused on one of the substrate particle. No Mg was detected. Combining the result from Figure 3.4 verifies that in-situ crystallization takes place within the porous structure of substrate, not on the top of the substrate.

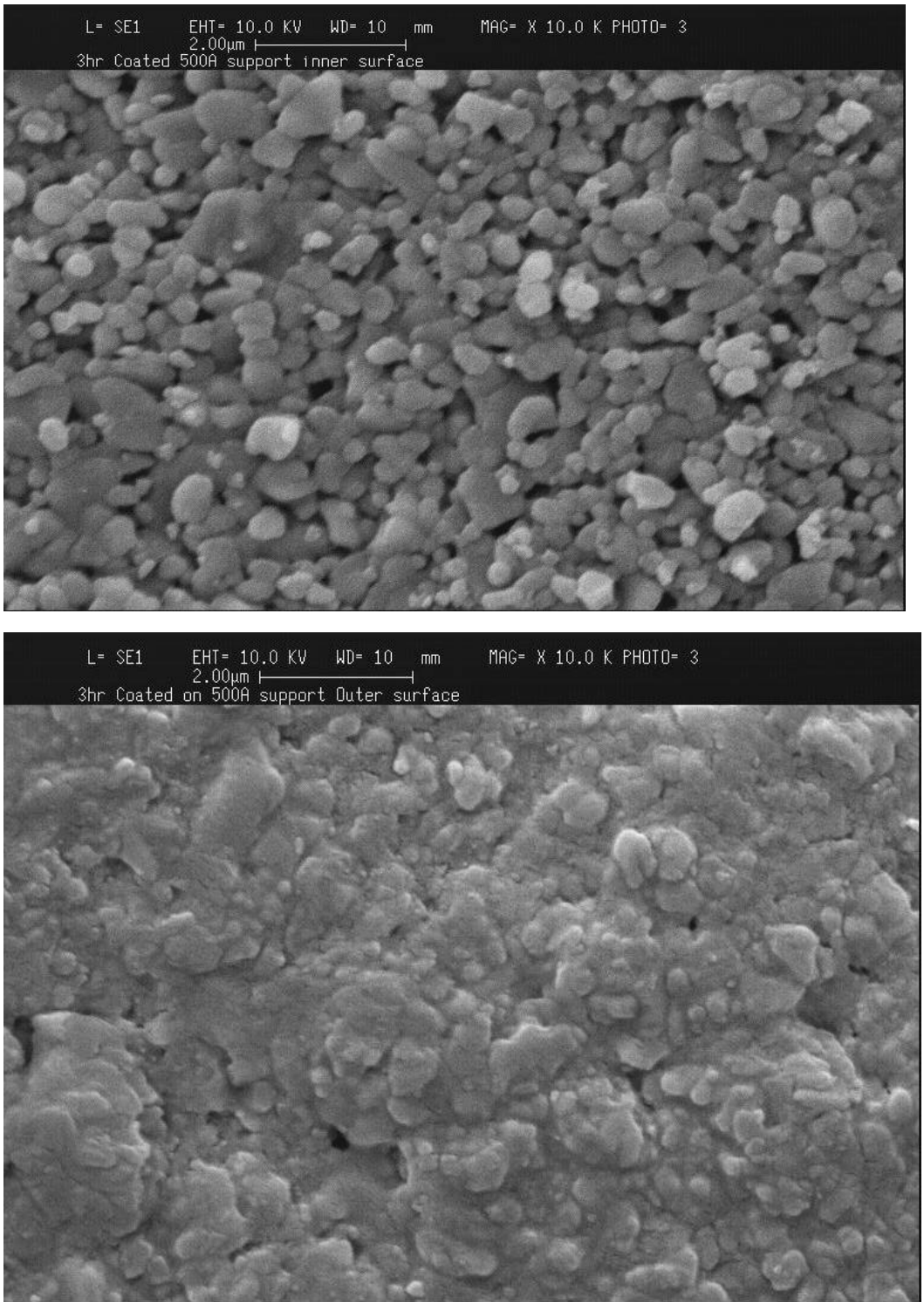

Figure 3.5 SEM Photomicrograph of 500Å substrate after in-situ crystallization of hydrotalcite: Inner tubular surface (top), and outer tubular surface (bottom). Pore plugging by hydrotalcite on the outer tubular surface is evident.

4. In-situ Crystallization on Inner Tubular Surface

In Sec. 3, we described the membrane synthesis technique involving in-situ crystallization as a first step. Then, in-situ crystal growth may be added as a 2nd step to reduce the residual pore opening prior to the post treatment by chemical vapor deposition (CVD). There we summarized the result of the in-situ crystallization on the outer surface of the 0.2ì and 500 A porous ceramic tubular substrates. The result was promising. In this section we summarize the result using this similar technique; however, the crystal was deposited on the inner tubular surface, instead of the outer surface. For a tubular ceramic membrane, it is a common practice to deposit the selective layer on the inner tubular surface for many technical reasons. Here we present the result on the deposition of the inner tubular surface.

Experimental

An experimental technique described in Sec. 3 for the deposition on the outer tubular surface is adapted here with minor modifications. The ceramic tube with one end sealed with epoxy was immersed into a $MgCl_2$ solution; then, the $AlCl_3$ solution is quickly added into the inner tubular space to initiate the crystallization in the interface immediately. The tube after this treatment is then subject to permeation flow rate measurement as an indication of the degree of the pore filling by the crystal. This in-situ crystallization was repeated up to 7 times to determine the improvement of the pore filling along with the number of the crystallization. In addition, to determine qualitatively the residual opening size, an initial flow measurement is conducted to quantify the % of flow contribution by the pore size in the order of >100Å. The pore size >100Å according to our previous experience is too big for developing a high quality CVD thin film. Thus, the degree of initial flow remained offers some guidance in terms of the requirement of the in-situ crystal growth as a second step.

Results

The permeation rate of the tubes with crystallization up to 7 times is summarized in Table 4.1 and Figure 4.1. The permeance of the membrane decreases along with the increase of the number of the crystallization. However, the initial flow measurement shown in Table 4.1 exhibits a similar degree of the remaining initial flow (i.e., ~50 to 60%) for the four samples prepared. Combining these results, one concludes that the crystal deposition after the 1st time likely settles on the top of the previous crystals to form an additional layer, instead of filling the residual gap. Thus, we conclude that one time in-situ crystallization may be adequate as seed for the subsequent growth to fill ~50% of the residual opening. The membrane sample is also examined under SEM as shown in Figures 4.2 & 4.3. In comparison with the bare substrate (see the top figure of Figure 3.6), the crystal formation on the inner membrane surface is evident. However, the penetration of the crystal cannot be deciphered by merely SEM examination. In fact the surface cracks as observed in these figures is supportive to the notion that the deposited layer >the 1st time may be too thick.

In a separate experiment with the 0.2 ì substrate, the initial flow measurement (Table 4.2 & Figure 4.4) shows a much-improved coverage by the crystal. However, the residual initial flow did not stabilize throughout the experimental study as shown in Figure 4.4, indicating that some artifact may be present. The result from this 0.2 ì substrate study will be repeated in the near future for selecting an ideal substrate for membrane synthesis in Year II.

Conclusions/Recommendation

- The in-situ growth with the 0.2 µ pore size will be completed for determining its suitability as substrate in comparison with the 500Å substrate.
- An surface analysis by EDX is currently undertaken. EDX analysis will be able to verify the presence of the hydrotalcite crystal and also determine the degree of the crystal penetration into the substrate. The results will be reported in a future quarterly report.

Table 4.1 Initial flow measurement of the 500A membrane after in-situ crystallization of hydrotalcites (8/27/2001)

HT-027-500A-1			HT-027-500A-3			HT-027-500A-5			HT-027-500A-7		
Time (hr)	Permeance	Initial Flow(%)	Time (hr)	Permeance	Initial Flow(%)	Time (hr)	Permeance	Initial Flow(%)	Time (hr)	Permeance	Initial Flow(%)
0.00	28.3	100	0.00	12.2	100	0.00	6.3	100	0.00	2.3	100
0.18	21.2	75	0.15	9.4	77	0.20	4.9	78	0.03	2.1	89
0.43	20.7	73	0.35	8.3	68	0.73	3.9	62	0.15	1.8	75
0.87	20.3	72	0.52	7.8	64	1.03	3.6	56	0.35	1.6	69
			1.02	7.0	57				0.53	1.5	65
			1.10	6.9	57				0.77	1.4	61
									0.98	1.4	58
Before water Permeation											
He permeance		28.6	He Permeance		12.3	He Permeance		6.4	He Permeance		2.0
N2 Permeance		11.7	N2 Permeance		5.0	N2 Permeance		2.6	N2 Permeance		0.8
Selectivity		2.44	Selectivity		2.47	Selectivity		2.46	Selectivity		2.60

Table 4.2 Initial flow measurement of the 0.2 micron membrane after in-situ crystallization

HT-026-0.2um-1			HT-026-0.2um-3		
Time (hr)	Permeance	Initial Flow(%)	Time (hr)	Permeance	Initial Flow(%)
0	107.0	88	0	59.4	100
0.01	90.0	74	0.07	40.6	68
0.12	86.4	71	0.22	37.8	64
0.41	61.7	51	0.37	37.0	62
1.04	43.0	36	0.59	32.2	54
1.32	34.6	29	1.36	122.8	22
1.51	33.6	28	2.09	3.8	6
			2.29	2.1	3

Before Permeantion

HT-026-0.2um-1		HT-026-0.2um-3	
He Permeance	121	He Permeance	58.5
N2 Permeance	61.5	N2 Permeance	32.5
Selectivity	1.96	Selectivity	1.8

Figure 4.1 Initial Flow of Hydrotalcite Membranes

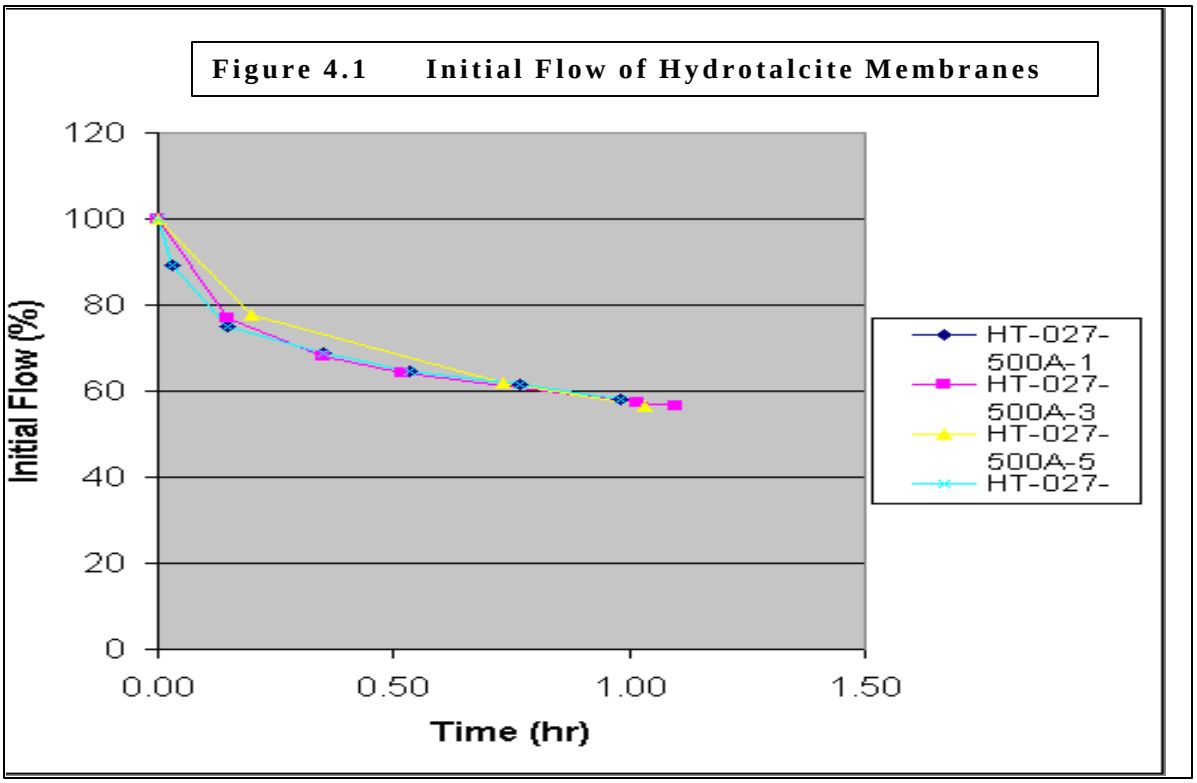

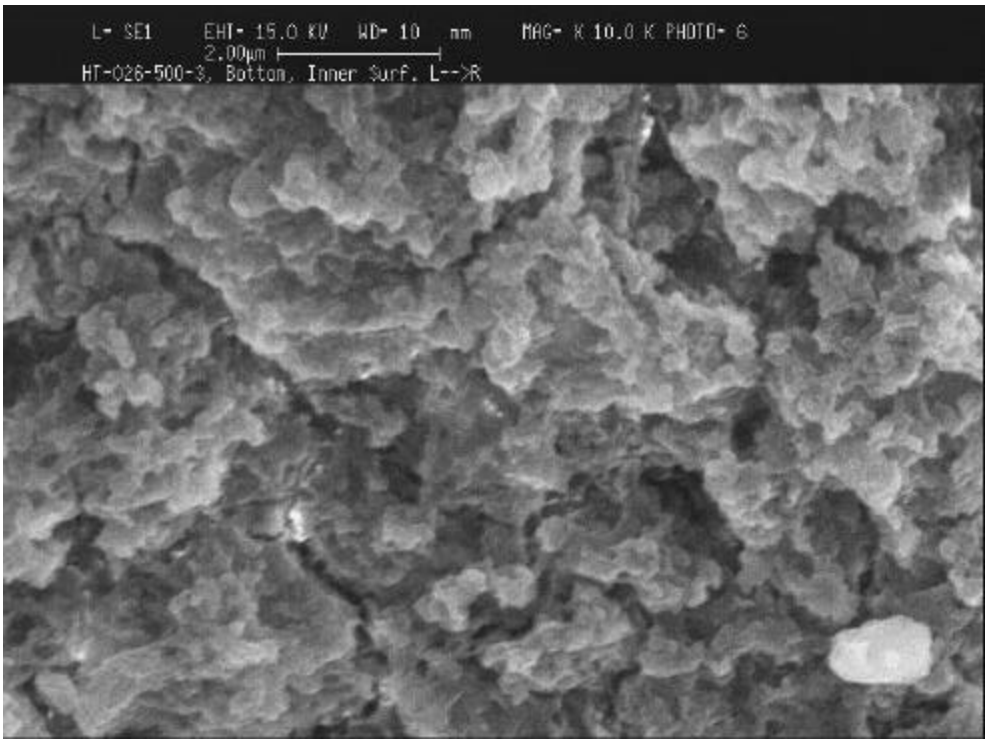

Figure 4.2 SEM photomicrograph of 500Å membrane deposited with hydrotalcite crystals via in-situ crystallization (3 times) – bottom of the inner tubular surface.

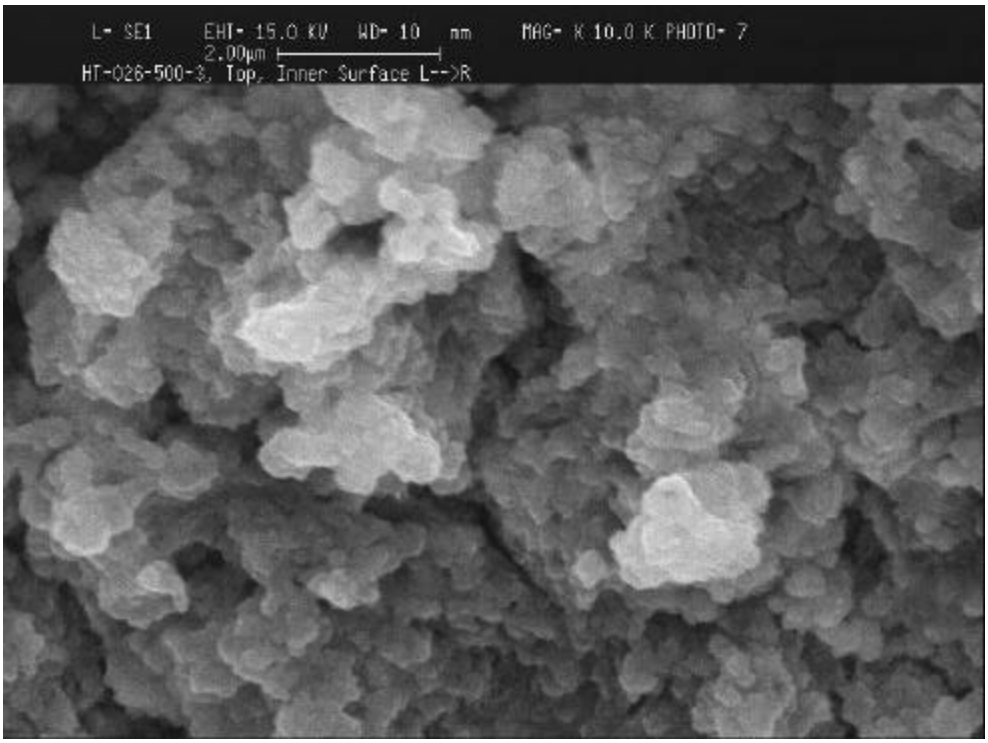

Figure 4.3 SEM photomicrograph of 500Å ceramic membrane deposited with hydrotalcite crystals via in-situ crystallization – top of the inner tubular surface.

Figure 4.4 Initial Flow Mesurement of 0.2 Micron Ceramic Membranes Deposited with Hydrotalcite via In-situ Crystalization

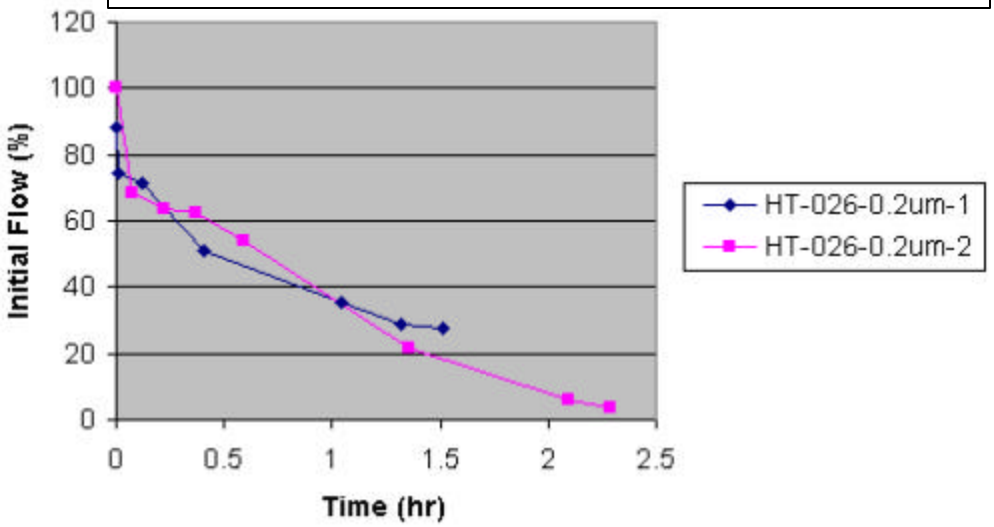

5. Feasibility Study on Backpatching with the Chemical Vapor Infiltration (CVI) Technique

To avoid non-selective transport through the voids between the single crystals and the base substrate, a chemical vapor infiltration (CVI) technique was proposed. The method has been developed and used by us in the development of our hydrogen selective membranes (SiO_2 and SiC based) [6,7]. The technique has been shown by us to be uniquely suited to the delivery of the precursor within the porous structure at a depth of 1 to 3Fm from the top surface of the substrate (instead of forming an additional layer on the top of the substrate). This unique capability is critical to the hydrotalcite membrane development. Deposition of an additional layer via CVI on the top of the membrane is not acceptable. Such deposition would indiscriminately cover and hence plug the CO_2 transport channels yielding significant reduction in CO_2 permeance and selectivity. Instead, it is necessary to plug only the inter-crystalline void spaces.

Experimental

1. To prove the technical feasibility during this project effort, M&P's existing CVI technique was employed without modifications in the precursor selection and deposition condition. The precursor used is TEOS, the deposition condition is 300EC. At this temperature, the TGA data obtained previously shows that part of the CO_2 transport channels are opened. However, the TEOS precursor molecule is too large to penetrate these openings in the range of 3 to 6D. In the feasibility tests, the CVI process was stopped when the reduction in He/O_2 carrier gas permeance was negligible with time.

Results

1. The CVI technique was demonstrated to reduce the residual pore openings of the membrane that remained following the in-situ crystallization discussed in Sec. 3 & 4. Table 5.1 shows that the permeance of a hydrotalcite membrane was reduced from 1.36 to 0.37 $m^3/m^2/hr/bar$ at 300EC, indicating that the selected CVI condition is sufficient to plug the residual pore openings following in-situ hydrotalcite crystallization.

2. SEM/EDX analysis of a 500D substrate following CVI shows that the silicon oxide deposition does not increase the layer thickness of the substrate membrane as evidenced by the grain structure of the top surface of the substrate shown in Figure 5.1. On the other hand, the EDX analysis shows that significant silicon deposition occurs in the first several microns inside the outer surface of the substrate. Thus, it is believed that the CVD technique employed here satisfies our performance requirement, specifically, penetration and plugging of the pore openings without indiscriminant deposition of an overlayer on the top of the existing substrate.

Recommendations/Conclusions

1. CVI of TEOS appears to be very promising. In the future, we will focus on the optimization of the CVI temperature, precursor vaporizer temperature, and the precursor. An ideal CVI temperature would be ca. 250EC at which none of the CO_2 transport channels are open. The 300EC deposition temperature selected in this project matched the conditions used in our in-house development of our core SiO_2-based ceramic hydrogen selective membrane technology. However, it is expected that these conditions are neither ideal nor optimized for the proposed hydrotalcite membrane. Also, to achieve the desired deposition conditions, it may be necessary to alter the precursor. Furthermore, the addition of additives that form pyroceram materials on low temperature calcination [8] could be used to cement the crystals to the pore walls of the substrate.

Table 5.1: Chemical Vapor Infiltration as a Backpatch for Hydrotalcite Membranes

Samples	Temperature [EC]	Helium Permeance [$m^3/m^2/hr/bar$]	Nitrogen Permeance [$m^3/m^2/hr/bar$]	Experimental He/N_2 Selectivity	Theoretical He/N_2 Selectivity
Before CVD	300	1.36	0.59	2.32	2.65
After CVD	300	0.37	0.16	2.23	2.65

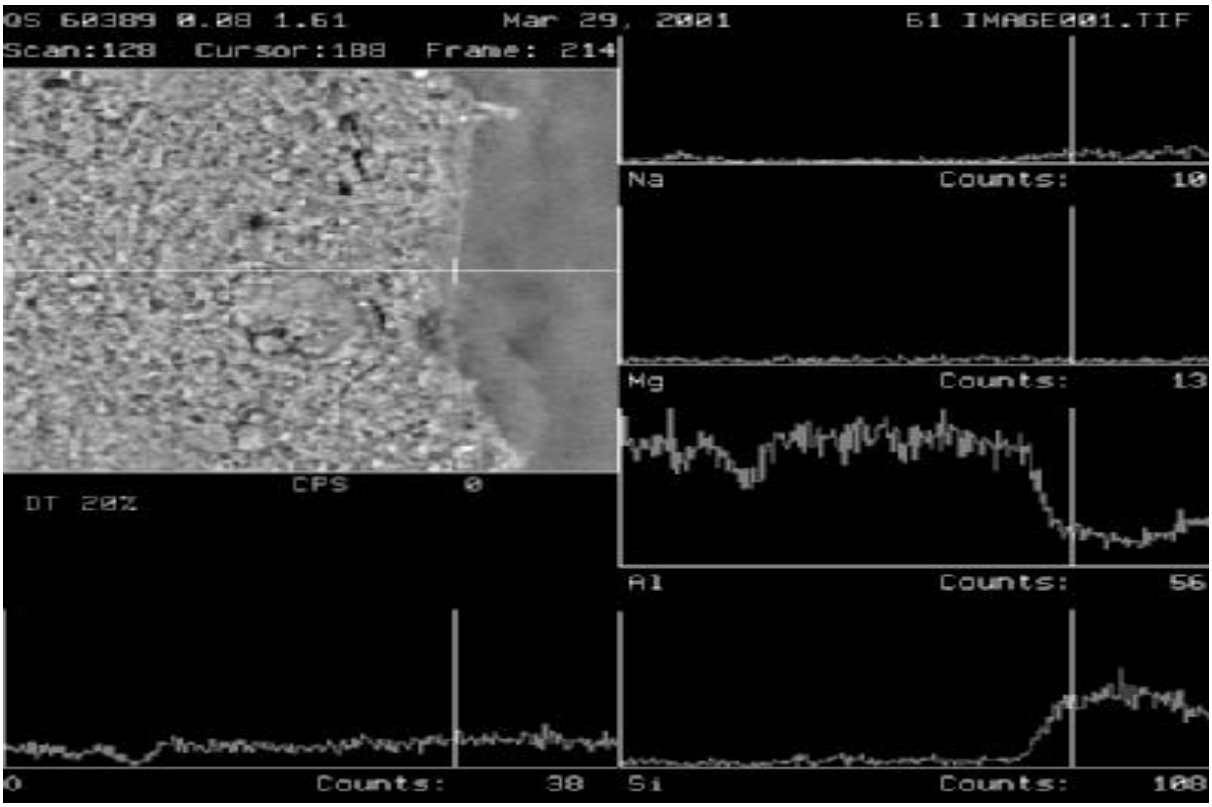

Figure 5.1 SEM Photomicrograph and EDX of the substrate after CVI. No visible layer deposition was observed from SEM. Significant Si precursor of CVD was observed on the inner tubular surface with very limited penetration into the substrate. The results indicate the CVD/I infiltrates into the porous structure of the substrate to form an ultra-thin effective membrane.

6. Performance Characterization of Hydrotalcite Membranes

Although the unique affinity to CO_2 of the hydrotalcite material has been well established in the literature, it was necessary that we confirm this affinity in the context of a membrane during this project to demonstrate the technical feasibility.

Experimental

1. Permeances of single components, including He, N_2 and CO_2, were measured at 300, 400 and 500EC to determine whether the membrane showed any affinity to CO_2. In our TEOS CVI based hydrogen (and helium) selective membranes, the permeance of N_2 (and CO_2) strictly results from Knudsen flow through defects in the SiO_2 infiltrated layer. Hence, a CO_2 permeance above that expected from Knudsen flow through the defects (which can be estimated from the N_2 permeance) must result from selective transport of CO_2 through the hydrotalcite crystals in the membrane.

2. Enhancement of the CO_2 transport by the hydrotalcite material will peak between 300 and 400EC according to the TGA study of this hydrotalcite material. The enhancement will diminish to negligible levels as the temperature is increased much beyond 400EC, since the hydrotalcite material begins to undergo phase change to a mixed oxide at these temperatures.

Results

1. At 300EC, the CO_2 permeance doubled as a result of the enhancement by the hydrotalcite embedded in the pores as shown in Table 6.1. The total CO_2 permeance was 0.26 $m^3/m^2/hr/bar$. It is estimated that the contribution to the CO_2 permeance from defects in the membrane is 0.14 $m^3/m^2/hr/bar$ based upon the measured nitrogen permeance and the Knudsen selectivity. Thus, 0.12 $m^3/m^2/hr/bar$ is the contribution to the CO_2 permeance due to transport of CO_2 through the CO_2 channels in the hydrotalcite crystals.

2. The enhancement at 400EC is reduced to 0.02 $m^3/m^2/hr/bar$ using a similar analysis as above. The enhancement is expected to be reduced under this experimental condition, since the low partial pressure of CO_2 does not promote adsorption of the CO_2 molecule at this temperature level. In addition, most of the hydroxyl groups available for forming CO_2 via the carbonate ion may be lost so that the injection of water is also likely to be necessary to promote CO_2 permeance enhancement (more discussion in Sec. 8).

Conclusions/Implications

1. Significant CO_2 permeance enhancement attributed to the active transport capabilities of the hydrotalcite material has been demonstrated experimentally. In addition, this enhancement decreases with increasing temperature, consistent with theoretical predictions at this experimental condition. During this project, membrane defects will be further reduced through the optimization of the CVI and in-situ crystallization techniques. In addition, an experimental set-up allowing us to perform the permeance in the presence of water at temperatures up to 500EC and pressures up to 100 psi will be pursued in this project Thus the full benefit of the CO_2 enhanced transport can be quantified

Table 6.1 Chemical Vapor Infiltration as a Backpatch for the Hydrotalcite Membrane. The Improvement in CO_2 Permeance due to Active Transport is shown at Various. The CO_2 Permeance in the Defects is Determined Using the Nitrogen Permeance and the Knudsen Selectivity. Permeance is in $m^3/m^2/hr/bar$.

	Temp [EC]	Pres [psi]	He Perm	N_2 Perm	CO_2 Perm	CO_2 Permeance due to Defects	***CO_2 Permeance due to Enhanced Transport***
Before CVD	300		1.36	0.59	-	-	-
After CVD	300		0.37	0.16	-	-	-
Post-CVD	300	15	0.36	0.17	0.26	0.14	***0.13***
Post-CVD	400	15	0.46	0.19	0.17	0.15	***0.02***
Post-CVD	500	15	0.84	0.36	0.29	0.29	***0.00***

7. Experimental Verification of CO_2 Reversibility and Hydrothermal Stability of Hydrotalcite Material

Hydrotalcite is known for its surface affinity to CO_2 in the presence of water at an intermediate temperature range, i.e., 150 to 450ºC. However, this affinity must be reversible via pressure and/or temperature swing in order to become a viable steady state CO_2 separation process through the membrane. Although knowledge regarding adsorption fundamentals of hydrotalcite materials suggests its reversibility, no literature study (i.e., experimental study) is available to verify this reversibility, particularly in the presence of water. As part of this project, an experimental program has been conducted for this purpose. Up to this point, we have completed the reversibility study using a TG/MS. Due to the limitation of the instrument, pressure swing between vacuum to <1 atmospheric pressure has been performed. The experimental study involving the pressure > 1 atm is presently under study using a high-pressure adsorption test rig.

Experimental

Powder hydrotalcite material was used in this study. A thermal gravimetric analyzer (TGA) with mass spectrum (MS) is used for this purpose. Step by step experimental condition is listed as follows:

(1) Evacuation for one day (below 50 mTorr)
(2) Ramp to 250ºC at 5ºC/min (P: vacuum)
(3) Isotherm 30 min at 250'C (P: Vacuum)
(4) Ramp to 150ºC at -5ºC/min (P: Vacuum)
(5) Isotherm 120 min at 150ºC (P: atmosphere with humidified CO_2)
(6) Ramp to 250ºC at 5ºC/min (P: Vacuum)
(7) Repeat (3) thru (6)

In addition a MS is used to analyze the off-gas on-line. Due to time lag resulted from the gas sample traveling from the balance in TGA to the MS, possible sample mixing, and other factors, MS is used here as a semi-quantitative tool to determine the relative composition of water vs CO_2 evolved to indicate the CO_2 affinity in the presence of water.

Results

Table 7.1 lists the experimental result with TGA using humidified CO_2 (at room temperature) as a carrier gas. The reversibility of CO_2 affinity is demonstrated in this 4-cycle study. Further in a separate study, MS analysis indicates the presence of both water and CO_2 in the off-gas. Thus, the reversibility in the presence of water is evident. In a previous run, a shorter adsorption cycle was performed, i.e., 30 instead of 120 minutes as in the above study. The result of this shorter cycle run is listed in Table 7.2. The result indicates that the degree of reversibility could be suffered if the adsorption time is insufficient.

Recommendations

In summary, in a membrane configuration with a steady state transport process, CO_2 is expected to adsorb and desorb reversibly to achieve the selective removal of CO_2 based upon the affinity of the hydrotalcite material.

- A similar reversibility study with the high-pressure adsorption unit is underway and will be completed in the near future to prove the reversibility at a high-pressure condition similar to the operating condition of the membrane.
- A similar experimental study as described here will be repeated for temperature at 200 to 500ºC to define the operating range of the hydrotalcite membrane.

Table 7.1 CO_2 Affinity in a Multiple Cyclic Study (with A Longer Adsorption Cycle)

Cycle	Wt loss via vacuum (%)	Wt gain via adsorption (%)
2nd	2.83	2.76
3rd	2.67	2.61
4th	2.57	2.52

Table 7.2 CO_2 Affinity in a Multiple Cyclic Study (with a Shorter Adsorption Cycle)

Cycle	Wt loss via vacuum (%)	Wt gain via adsorption (%)
2nd	2.00	1.75
3rd	1.69	1.66
4th	1.21	0.50

8 Surface Study of CO_2 Affinity vs Temperature using Hydrotalcite Bulk Materials

Surface characterization of the hydrotalcite material is critical to the design of an optimum hydrotalcite membrane for CO_2 separation from water gas shift reaction. This section summarizes our surface analysis using IR spectroscopy to determine the coordination of CO_2 vs. temperature, the role of water (or hydroxyl group), and its structure stability vs. temperature. A thermal evolution pattern is proposed, supported by the FTIR, DRIFTS and TGA/MS results. In year II, we will begin to (i) define the operating temperature range for the hydrotalcite membrane, and (ii) determine the effect of the Al/Mg ratio or cation substitution other than magnesium

8.1 Proposed Mechanism for Thermal Evolution Pattern of Hydrotalcite

Based upon the results of in-situ DRIFTS coupled with TG/DTA/MS studies, we are proposing the following model for thermal evolution of hydrotalcite under an inert atmosphere. Five stages are identified as follows:

Stage A - the original hydrotalcite sample at room temperature;
Stage B - developed by the removal of loosely held interlayer water in the Stage A at the temperature range of 70 to 190EC;
Stage C - evolved from the Stage B by the removal of (i) OH^- groups bonded with Al^{3+} at the temperature range of 190 to 280EC and (ii) OH^- groups bonded with Mg^{2+} at the temperature range of 280 to 405EC;
Stage D - achieved by decarbonation of Stage C at the temperature range of 410 to 580EC;
Stage E - obtained when the temperature exceeds 580EC.

We have quantitatively determined the changes of the functional groups of the hydrotalcite sample along with the temperature increase (see Sec. 8.3 to 8.5), and proposed a model to describe these changes. In order to verify the model we proposed and determine how there changes influence the LDH structure, further study with an in-situ HTXRD is planned.

8.2 FT-IR Study of Hydrotalcite at Room Temperature

Figure 8.1 showed the comparison with DRIFTS and FT-IR results of hydrotalcite at room temperature. It shows that all the signals of the DRIFTS for the hydrotaclite coincide with those from FT-IR. The intensities of DRIFTS signals are strong enough to clearly identify all the species in the hydrotalcite. Based on the literatures for FT-IR on the hydrotalcite, we assigned all the DRIFTS signals to the corresponding species as below:

(1) DRIFTS signal at ~3470 cm^{-1} was assigned to OH^- group vibration in the hydrotalcite sample;
(2) DRIFTS signal at ~3070 cm^{-1} was assigned to hydrogen bonding between water and carbonate in the interlayer of the hydrotalcite;
(3) DRITS signal at ~1620 cm^{-1} was assigned to H_2O bending vibration of interlayer water in the hydrotalcite sample;
(4) DRIFTS signals at $<_3$=1370 cm^{-1}, and $<_4$=680 cm^{-1} at room temperature were assigned to CO_3^{-2} group vibration bands in the hydrotalcite sample, which behave like in the water solution, i.e., $<_3$=1415 cm^{-1}, $<_2$=880 cm^{-1}, and $<_4$=680 cm^{-1}. In this case, no splitting of $<_3$ band and $<_1$ mode vibration at ~1080 cm^{-1} were observed, which usually were generated from the symmetry degradation and the interaction between CO_3^{-2} and Mg^{2+}. This means that CO_3^{-2} in the hydrotalcite sample has no or very weak direct interaction with positive ions, such as Mg^{2+} and Al^{3+} at room temperature.

Based upon the above assignments, we can characterize the surface functional group change along with the temperature increase. The results obtained in this quarter are summarized in the rest of this report.

8.3 DRIFTS Study of Hydrotalcite at High Temperature

According to the above assignments, we can use in-situ DRIFTS technique to characterize the evolution process of hydrotalcite, i.e., the changes of the functional groups as a function of temperatures. The in-situ DRIFTS results are shown in Figure 8.2. The hydrotalcite sample was treated in Ar with continuously increasing temperature to 560EC, and the in-situ DRIFTS was recorded at each temperature under an isothermal condition for a period of ~2 minutes with an 20EC interval. From Figure 3, several conclusions can be drawn as follows:

(i) The intensities of DRIFTS bands for interlayer water at 3070 cm^{-1} and 1620 cm^{-1} gradually decrease with the increase of temperature, and disappear at 220EC. This means that more and more interlayer water in the hydrotalcite is removed with the increase of temperature, and completely removed at 220EC.

(ii) The intensity of OH^- vibration signal at 3470cm^{-1} begins to decrease at temperature of 190EC and disappears at 440EC, which suggests that the partial dehydroxylation of the hydrotalcite occurs at 190EC, and completed at 440EC.

(iii) The splitting of signal at 1370 cm^{-1} for $<_3$ vibration of CO_3^{-2} to two signals, i.e., 1530cm^{-1} and 1350cm^{-1}, at temperatures higher than 170EC and (ii) appearance of $<_1$ at 1090cm^{-1} which is infrared inactive in the free CO_3^{-2} at temperatures higher than 340EC, indicate that symmetry of the hydrotalcite sample becomes worse after thermal treatment. It is interesting to observe that the intensity of the signal at a lower wavenumber (~1350cm^{-1}) decreases and the intensity of the signal at a higher wavenumber (~1530cm^{-1}) increases with the increase of temperature. Furthermore, the position of these two split signals becomes closer with the increase of temperature, which behaves more like CO_3^{-2} in $MgCO_3$ as shown in Figure 3. The $<_3$ vibration of CO_3^{-2} in $MgCO_3$ was split to two signals, i.e., 1499 cm^{-1} and 1425cm^{-1}, and the $<_1$ vibration band of CO_3^{-2} in $MgCO_3$ was observed at 1100 cm^{-1} due to the symmetry degradation of CO_3^{-2} in $MgCO_3$. These results indicate that after removal of the interlayer water and OH^- groups at high temperatures (170 to 400EC), CO_3^{-2} is directly bonded with Mg^{2+} to form $MgCO_3$-like species. This conclusion is also confirmed by the fact that the decarbonation temperature range of 410 to 560EC for the hydrotalcite shown in Figure 8.2 is quite similar to the decomposition temperature range of 400EC to 560EC for $MgCO_3$, shown in Figure 8.3.

Figure 8.4 is a semi-quantitative interpretation of the insitu DRIFTS (shown in Figure 8.2), indicating the fraction of each particular species that is removed at a given temperature. The calculations are based on the peak area of the corresponding species, i.e., 3470cm^{-1} represent OH^- group, 3070cm^{-1} and 1620cm^{-1} represent interlayer water, and 1370cm^{-1} at lower temperatures or 1530 cm^{-1} and 1350cm^{-1} at higher temperatures represent CO_3^{-2}. For the interlayer water, it begins to release at 70EC and is completely lost at 220EC. For OH^- groups, the big difference in slope between the temperature range of 190 -250EC and that of 250 - 430EC suggests that there are two different kinds of OH^- groups in the hydrotalcite sample. One kind of OH^- group is removed at the temperature range of 190 - 250EC, and another kind of OH^- group is removed at the temperature range of 250 - 430EC. A small amount of CO_3^{-2} is removed at the temperature range of 180 - 240EC (~2wt%), and most of CO_3^{-2} is removed at the temperature range of 390 - 560EC (~98%), which is also confirmed by in-situ MS, as shown in Figure 5. A small amount of CO_2 from the hydrotalcite was detected at the temperature range of 190 - 280EC, and most of the CO_2 was detected at the temperature range of 370 - 600EC.

8.4 TGA Study on 1st Weight Loss Peak

In-situ DRIFTS is a powerful technique to monitor the changes of the functional groups in the hydrotalcite sample during the thermal treatment. However, for precise quantitative purpose, TG/DTA is one of the best choices. Figure 8.6 shows the weight change and the heat flow of the hydrotalcite sample as a function of temperature under inert gas atmosphere. Combined with the results of in situ DRIFTS in Figure 8.2, we know that the first weight loss, ~14wt% by weight, at the temperature range of 70 - 190EC should be from the interlayer water in the hydrotalcite plus a small amount of CO_2 and H_2O from OH^- group. The theoretical percentage by weight of the interlayer water in the hydrotalcite can be calculated based up the following reaction,

$$Mg_{0.76}Al_{0.24}(OH)_2(CO_3)_{0.12}0.43H_2O = Mg_{0.76}Al_{0.24}(OH)_2(CO_3)_{0.12} + 0.43H_2O \ (70 - 190EC)$$

The total molecular weight of $Mg_{0.16}Al_{0.24}(OH)_2(CO_3)_{0.12}0.43H_2O$ is 73.89, and the total weight of the interlayer water in the hydrotalcite is 7.74 (0.43x188 = 7.74). So, the theoretical percentage of interlayer water in the hydrotaclite is 10.48% by weight (7.74/73.89 = 10.48). The difference (3.52% by weight) should be attributed to the contribution of CO_2 and H_2O from OH^- group because there indeed is a small amount of CO_2 and H_2O from OH^- group which were removed at the temperature range of 70 - 190EC, as shown in Figure 8.3. At the same time, DTA result shows that only a small amount of heat (no heat flow peak was observed at the temperature range of 70 - 190EC) is needed for the first weight loss, which indicates that the interlayer water physically adsorbed in the nano-slits between the layers of the hydrotalcite.

8.5 TGA Study on 2nd and 3rd Weight Loss Peaks

The second weight loss peak (~6.7% by weight) occurs at 190 - 280EC, which is accompanied by two heat flows (endothermic) with their peaks at 205 (small shoulder peak) and 255EC. The third weight loss (~15.4% by weight) peak occurs at 280 - 405EC, which is accompanied by a heat flow (endothermic) with its peak at 340EC. According to the above DRIFTS results in Figure 8.2, there are two kinds of OH^- groups, which are removed at the temperature range of 190 - 430EC, i.e., one at 190 - 250EC, and another at 250 - 430EC. Therefore, the second weight loss at 190 - 280EC, and the 3rd weight loss at 280 - 405EC are attributed to the removal of two different kinds of OH^- group, which may be associated with Al^{3+} and Mg^{2+} respectively. In order to clarify the properties of these two kinds of OH^- groups, we performed TG/DTA experiments on pure $Al(OH)_3$ and $Mg(OH)_2$ samples. The results are shown in Figure 8.7 and 8.8. Figure 8.7 shows that the OH^- group associated with Al^{3+} was lost at the temperature range of 190 - 315EC, and two heat flows (endothermic) were observed associated with this loss. Figure 8.8 showed that the OH^- group associated with Mg^{2+} was removed at the temperature range of 290 - 405EC, and only one heat flow (endothermic) was observed in this case. Compared Figure 8.6 with Figures 8.7 and 8.8, one can conclude that the weight loss and the thermal behavior of the hydrotalcite in Figure 8.6 at the temperature range of 190 - 200EC are nearly identical to those of $Al(OH)_3$ (Figure 8.7). By the same token, the weight loss and the thermal behavior of the hydrotalcite in Figure 8.6 at the temperature range of 280 - 405EC are similar to those of $Mg(OH)_2$ shown in Figure 8.8. These results mean that the second weight loss (~6.7% by weight) in Figure 8.6 at the temperature range of 190 - 280EC is likely resulted from the removal of water from the OH^- group bonded with Al^{3+} and the third weight loss (~15.4wt%) in Figure 8.6 at temperature range of 280 - 405EC is the removal of H_2O from the OH^- group bonded with Mg^{2+}. These assignments were further supported with the theoretical calculation presented in Sec. 8.6.

8.6 Theoretical Calculation on Weight Loss

Quantitative weight loss vs temperature can be estimated based upon the theoretical calculation with the chemical formula of hydrotalcite incorporated with the evolution behavior discussed in Sec. 8.3 to 8.4. The weight loss for the OH^- bonded with Al^{3+} in the hydrotalcite was calculated based on the following reactions:

$$Mg_{0.76}Al_{0.24}O_{0.36}(OH)_{1.28}(CO_3)_{0.12} = Mg_{0.76}Al_{0.24}O_{0.36}(OH)_{1.28}(CO_3)_{0.12} + 0.36\ H_2O\ (190 - 280EC)$$

by assuming that Al^{3+} only bonded with OH^- because in-situ DRIFTS results in Figure 8.2 already show that CO_3^{-2} only bonded with Mg^{2+}, and there is almost no interactions between CO_3^{-2} and Al^{3+}. Thus, the percentage for the loss of the OH^- bonded with Al^{3+} in the hydrotalcite is 8.77% by weight (0.36x18/73.98=8.77%). The experimental value (6.7%) is slightly lower than the theoretical value (8.77%) due to the removal of a small amount of OH^- group bonded with Al^{3+} at the lower temperature range of 70 - 190EC, as shown in Figure 8.3. The large heat flow in this case also confirms that the OH^- group chemically bonded with the higher valence element, i.e., Al^{3+}.

The percentage for the loss of the OH^- group bonded with Mg^{2+} in the hydrotalcite was calculated based on the following reaction:

$$Mg_{0.76}Al_{0.24}O_{0.36}(OH)_{1.28}(CO_3)_{0.12} = Mg_{0.76}O_{0.64}Al_{0.24}O_{0.36}(CO_3)_{0.12} + 0.64\ H_2O\ (280 - 405EC)$$

The result shows that the percentage for the loss of the OH^- bonded with Mg^{2+} in the hydrotalcite was 15.5% by weight (0.46x18/73.98 = 15.59%), which is almost same as the experimental value of ~15.4%.

The last weight loss (~5.9%) at the temperature of 405 - 580EC shown in Figure 8.6, was attributed to the removal of CO_2 from CO_3^{-2}. The theoretical percentage of the loss of CO_2 from CO_3^{-2} in the hydrotalcite was calculated based on the following reaction:

$Mg_{0.76}O_{0.64}Al_{0.24}O_{0.36}(CO_3)_{0.12} = Mg_{0.76}O_{0.76}Al_{0.24}O_{0.36} + 0.12CO_2$ (405 - 580EC)

The result shows that the theoretical percentage for the loss of CO_2 is 7.15% by weight (0.12x44/73.89=7.15%). The experimental value (~5.9%) is slightly lower than the theoretical value (7.15%) at the temperature range of 405 - 580EC due to a small amount of CO_2 already removed at a lower temperature range, i.e, 190 - 250EC (see Figure 8.4). Thus, the quantitative information obtained here is consistent with the thermal behavior inferred from the DRIFTS and TGA/DTA study.

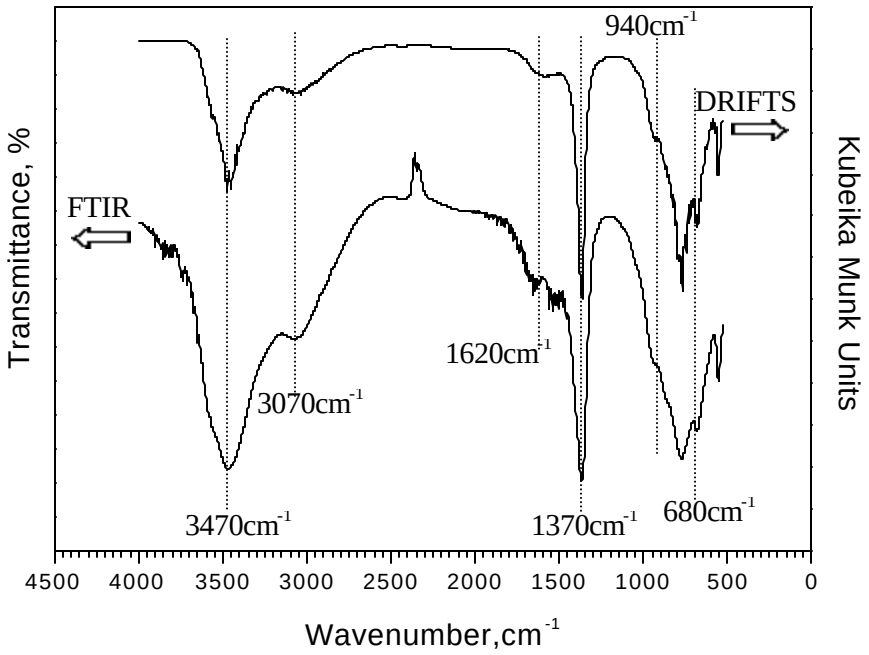

Figure 8.1 Comparison of FT-IR with DRIFTS Results on Hydrotalcite Material

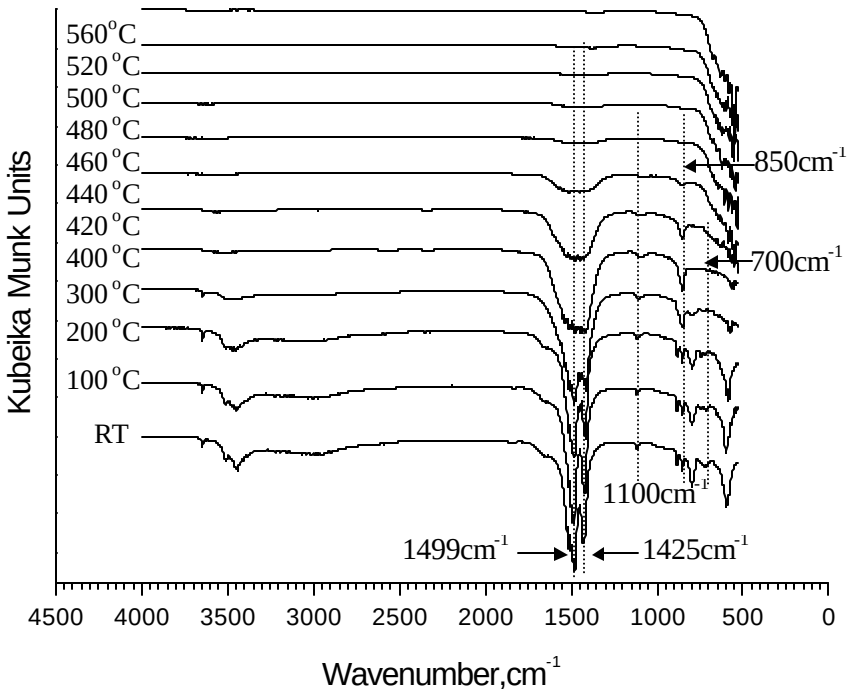

Figure 8.2 DRIFTS Results on Hydrotalcite Material at 25 to 560EC

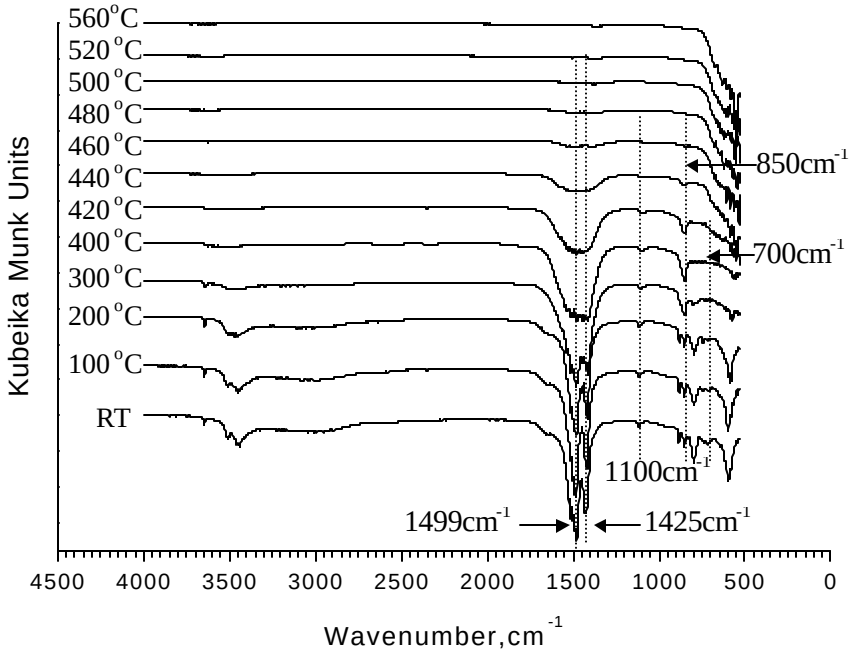

Figure 8.3 DRIFTS Results on $MgCO_3$ for Comparison with the Hydrotalcite Results Shown in Figure 8.2.

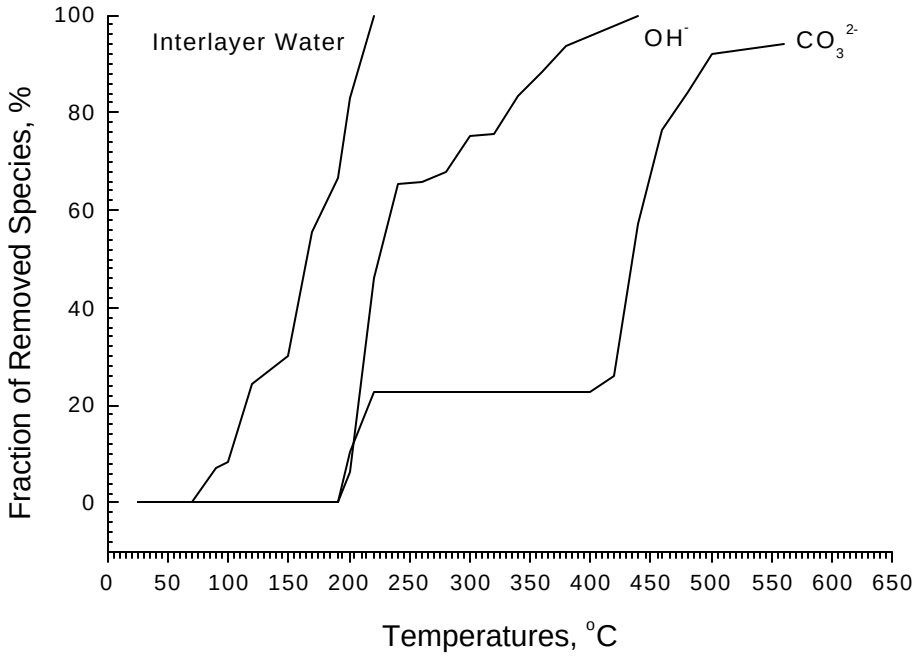

Figure 8.4 Weight Loss vs Temperature for Each Components Evolved from Hydrotalcite as a result of Thermal Treatment

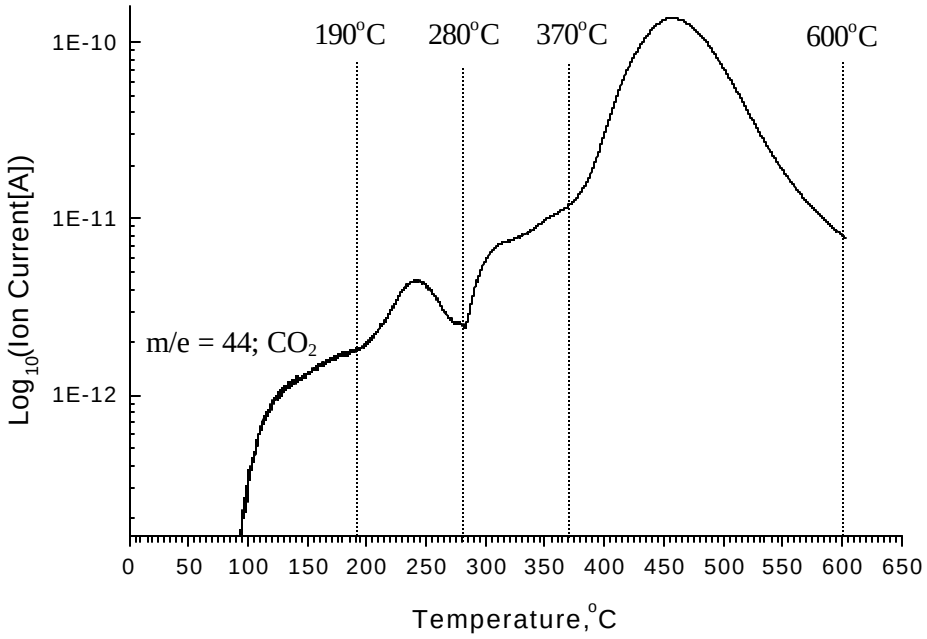

Figure 8.5 Mass Spectrum vs Temperature for Off-gas from Hydrotalcite at 25 to 600EC

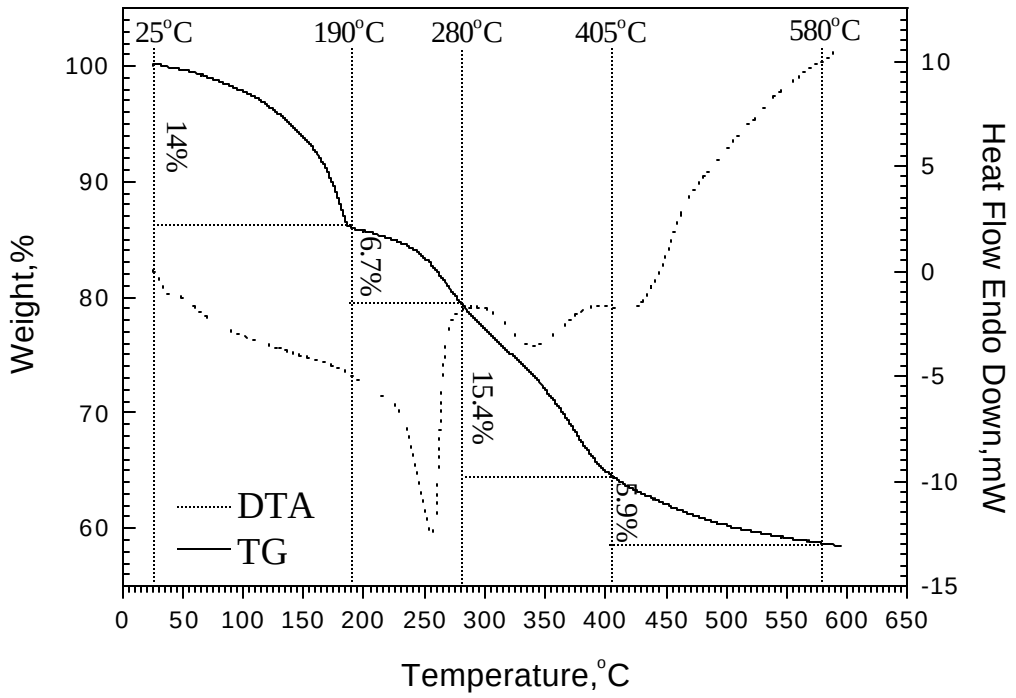

Figure 8.6 TG/DTA Results on Hydrotalcite

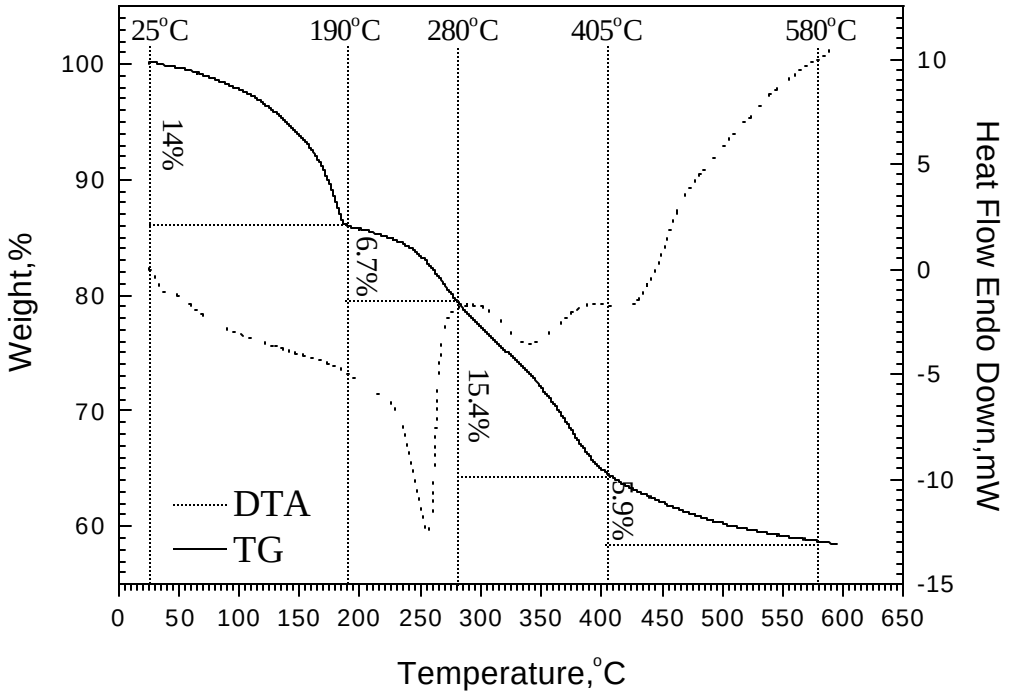

Figure 8.7 TG/DTA for $Al(OH)_3$ for Comparison with Hydrotalcite Results

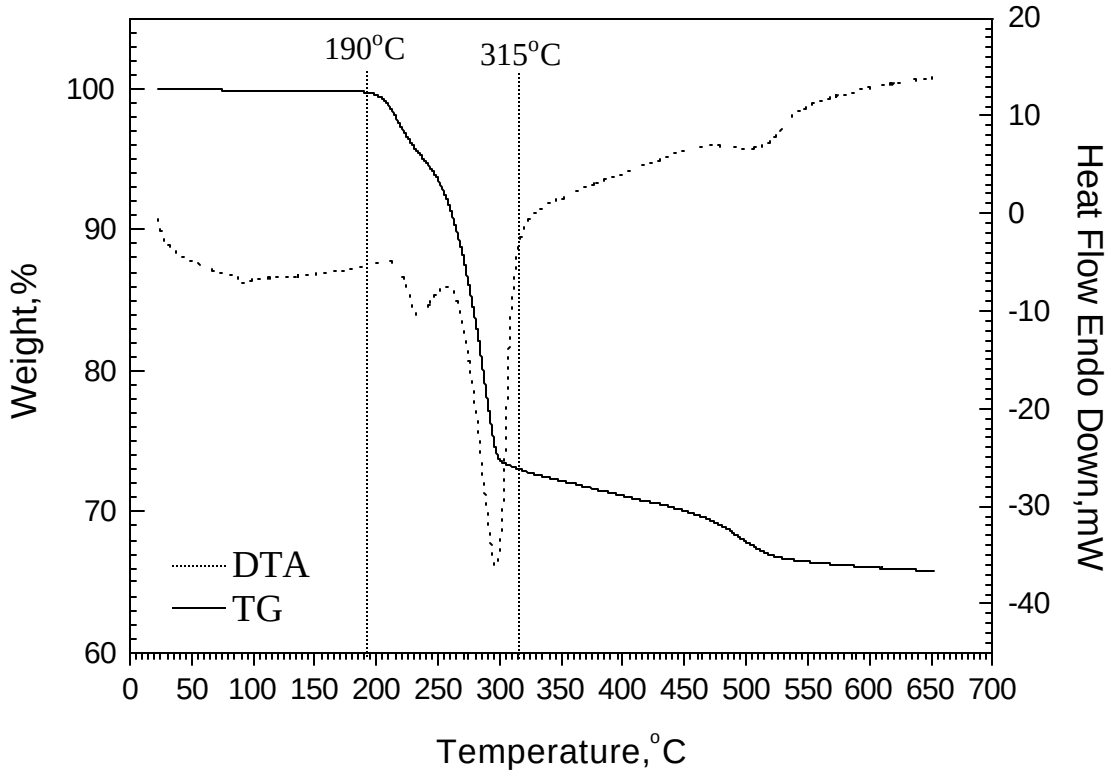

Figure 8.8 TG/DTA of $Mg(OH)_2$ for Comparison with Hydrotalcite Results

REFERENCES CITED

1. Aramendia, M.A., et. al., J. Mater. Chem., 9, 1603, (1999).
2. Kanezaki, E., J. Material Science Letters, 17, 371, (1998).
3. Reichle, Anionic Clay Minerals, Chemtech, January 1986, p. 58.
4. Tsuji, M., G. Mao, T. Yoshida, and Y. Tamaura, J. Mater. Res., 8, 1137(1993).
5. Roelofs, J.C. A.A., D. J. Lensveld, A. J. van Dillen, and K. P. de Jong, J. Catalysis , 203, 184(2001).
6. Wu., J.C.S., Sabol, H.K., Smith, OW., Flowers, D.F., Liu, P.K.T., J. Membrane Science,96, 275 (1994).
7. Liu, P.K.T., and Wu, J.C.S., U.S. Patent 5.415.891, May 16(1995).
8. Corning Ceramic Bulletin on Pyroceram.